Structural origin of magnetic biased field in NiMn/NiFe exchange coupled films

Bunsen Y. Wong
Department of MSE, Carnegie Mellon University, Pittsburgh, Pennsylvania 15213

Chiharu Mitsumata
The Moka Branch, HMRL, Hitachi Metals Ltd. Moka, 18 Matsuyama-cho, Moka, Tochigi, 321-43 Japan

Shiva Prakash
Applied Magnetics Corp., 75 Robin Hill Road, Goleta, California 93117

David E. Laughlin[a)]
Department of MSE, Carnegie Mellon University, Pittsburgh, Pennsylvania 15213

Toshio Kobayashi
The Moka Branch, HMRL, Hitachi Metals Ltd. Moka, 18 Matsuyama-cho, Moka, Tochigi, 321-43 Japan

(Received 30 November 1995; accepted for publication 6 February 1996)

The factors which determine the strength of the magnetic biased field in NiMn/NiFe exchange biased system have been examined. It was found that a strong NiFe (111) texture and columnar growth are essential to obtaining a high exchange field as they facilitate epitaxy between the NiFe and NiMn layers. The application of an amorphous Ta nucleation layer and substrate biasing during NiFe deposition have been found to promote these structures. Fcc NiMn replicates the (111) texture through epitaxial growth on NiFe according to a cube on cube orientation relationship. Upon annealing, atomic ordering takes place in the NiMn layer and gives rise to an exchange biased field. However, a fully $L1_0$ ordered structure cannot be achieved at the NiMn/NiFe interface due to the stabilizing effect of fcc NiFe. Away from the interface, the transformation proceeds and the ordered tetragonal unit cell creates a lattice strain within the NiMn film. This strain is relieved by twinning within the NiMn grains of the film. The strength of the exchange field has been found to be closely associated with the density of twins and their proximity to the NiMn/NiFe interface. © *1996 American Institute of Physics.* [S0021-8979(96)04410-3]

I. INTRODUCTION

The introduction of magnetoresistive (MR) sensors as flux sensing elements in magnetic storage technology has expedited the increase in the areal bit density.[1] The main advantage of MR heads is their high sensitivity. The higher output signal allows the application of thinner medium with smaller track width and bit length, which facilitate higher data storage density. In addition, the signal that is produced is proportional to the flux change (Φ) along the data track in the media instead of rate of change $d\Phi/dt$. This favors the use of disks with lower form factor thus reducing access time.

In order to achieve high sensitivity in conventional NiFe anisotropic magnetoresistive (AMR) heads, two bias fields are required (Fig. 1). The transverse bias field enables the sensor to operate in the linear response region with high sensitivity whereas the longitudinal field stabilizes the domain structure within the NiFe film by suppressing the Barkhausen noise from domain wall motion. The transverse bias field can be implemented in a variety of ways.[2] The longitudinal bias field is often realized by depositing an exchange layer, usually antiferromagnetic, on the NiFe film.[3,4] Hence, an exchange bias is induced in the magnetic layer.[5–8] Exchange biasing is also prominently featured in giant-magnetoresistive (GMR) spin-valve sandwiched structures.[9,10] The exchange layer is used to pin the magnetization in one of two NiFe layers and allows the second layer to rotate freely. A high exchange field is essential to ensure that the magnetization within the pinned layer is insensitive to the external flux.

The strength of the exchange bias field is determined by a number of factors. Foremost is the anisotropy field of the exchange layer material. A high anisotropy field provides not only a large exchange field but also a high blocking temperature. The field is also very sensitive to the processing conditions which ultimately determine the exchange coupling across the exchange layer/NiFe interface.[11] A number of materials have been suggested as exchange layer candidates, e.g., FeMn,[12–14] NiMn,[15] TbCo,[16,17] NiO,[18] and CoNiO.[19] FeMn and TbCo are known to provide high exchange field in the as-deposited structure, but since they are susceptible to corrosion, degradation of the device over time is possible. On the other hand, NiO and CoNiO are chemically stable, but their low blocking temperature and crystalline anisotropy remain as hindrances to their application. Exchange biasing utilizing NiMn has been shown to possess both high blocking temperature and bias field.[20] At room temperature, bulk NiMn is antiferromagnetic with the CuAu–I ($L1_0$) ordered tetragonal crystal structure (Fig. 2) and it possesses a Néel temperature of nearly 800 °C.[21–24] High exchange bias field in the NiFe film can be obtained through postdeposition annealing. The field strength is closely associated with the deposition and annealing conditions.

[a)]Electronic mail: d10p@andrew.cmu.edu

 0021-8979/96/79(10)/7896/9/$10.00

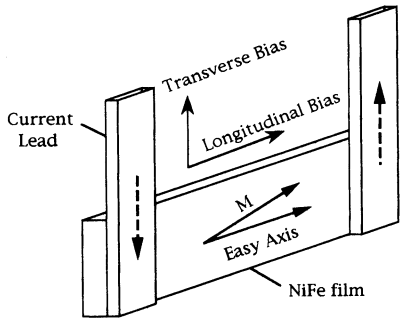

FIG. 1. Schematic of a AMR sensor with direction of the bias fields indicated.

In this work, we investigate the microstructural origin of the exchange field as a path to further the understanding of the exchange phenomenon between NiMn and NiFe. The primary goal is to discern and comprehend the microstructural features contributing to high exchange bias field. To accomplish this, the deposition conditions were varied in order to induce a range of exchange fields in various samples. The structure of these multilayer samples was then examined so as to determine: *(1) the microstructure across the NiMn/NiFe interface and, (2) the crystal structure of the respective layers* and to determine their possible relations to the strength of the exchange field.

II. EXPERIMENTAL PROCEDURES

Three series of specimens were deposited onto an Al_2O_3 underlayer which had been sputtered on Si substrates.

(i) *40 nm NiMn.* A single NiMn layer to be used for determination of the crystal structure.

(ii) *10 nm Mo/40 nm NiMn/30 nm NiFe/10 nm Ta/20 nm NiFeCr.* A NiFeCr layer was first deposited as the soft adjacent layer. The effect of substrate biasing during the deposition of the Ta underlayer was studied for specimens A–D.

(iii) *10 nm Mo/40 nm NiMn/35 nm NiFe/10 nm Ta.* The role of substrate biasing during deposition of NiFe was investigated for specimens E and F.

TABLE I. Substrate bias voltage used in deposition of the respective layers and the magnitude of the exchange bias field.

Specimen	Ta (V)	NiFe (V)	NiMn (V)	H_{ex} (Oe)
A	0	−30	−10	40
B	−50	−30	−10	42
C	−100	−30	−10	32
D	···	−30	−10	10
E	0	−80	−10	68
F	0	−30	−10	11
NiMn	···	···	−10	···

The substrate bias applied during deposition for the various layers is listed in Table I. All specimens were sputtered with Ar gas pressures between 5 and 20 mTorr and with forward powers between 400 and 1000 W. An external field of 60 Oe was applied during deposition. The NiFe layer was deposited in two steps. After the deposition of NiFe1, the chamber vacuum was disrupted. A light sputter etching was administered to remove any surface oxide before depositing the NiFe2, NiMn, and Mo layers. All specimens were annealed at 300 °C for 6 h.

The overall texture of the films was determined with a Rigaku θ–2θ x-ray diffractometer. Film microstructure was examined by both conventional transmission electron microscopy (TEM) (Philips 420T) and high-resolution transmission electron microscopy (HRTEM) (JEOL 4000EX).

III. RESULTS

(i) *40 nm NiMn.* The diffraction spectrum is shown in Fig. 3. Both (111) and (200) peaks are present. Since there is no bifurcation of the (200) peak into (002) and (200) peaks, the film is composed of mainly the fcc phase. The half width of the diffraction peaks is about 1° which reflects the presence of large NiMn grains.

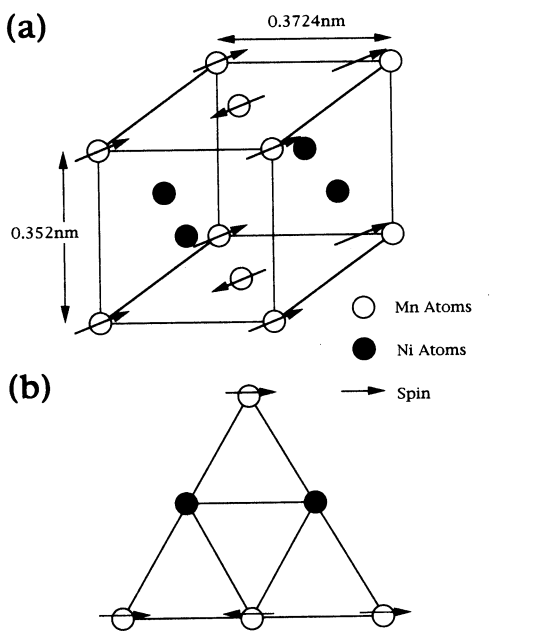

FIG. 2. (a) Schematic of the NiMn $L1_0$ ordered antiferromagnetic crystal cell. (b) Atomic arrangement of the (111) plane.

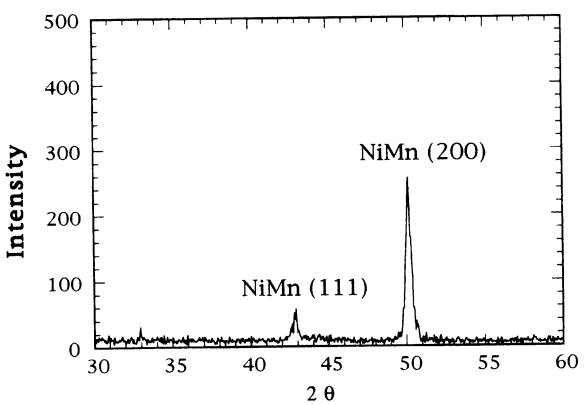

FIG. 3. X-ray diffraction spectrum of $NiMn/Al_2O_3/Si$.

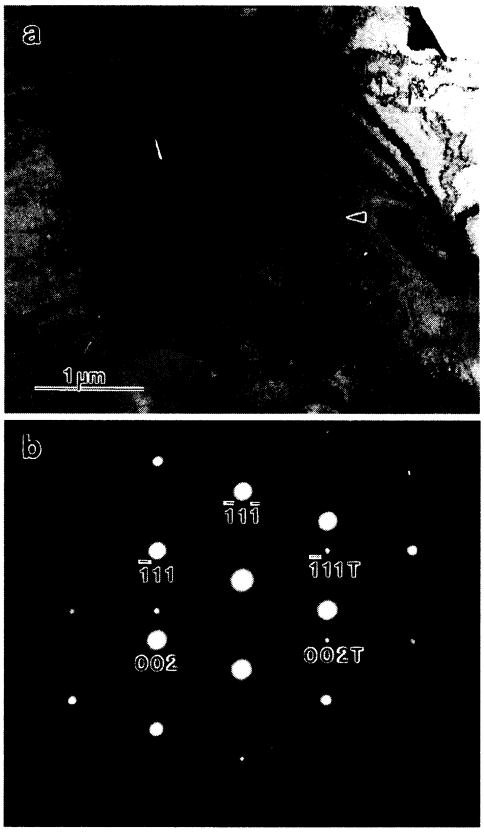

FIG. 4. (a) BF image and (b) corresponding SAD pattern of NiMn film.

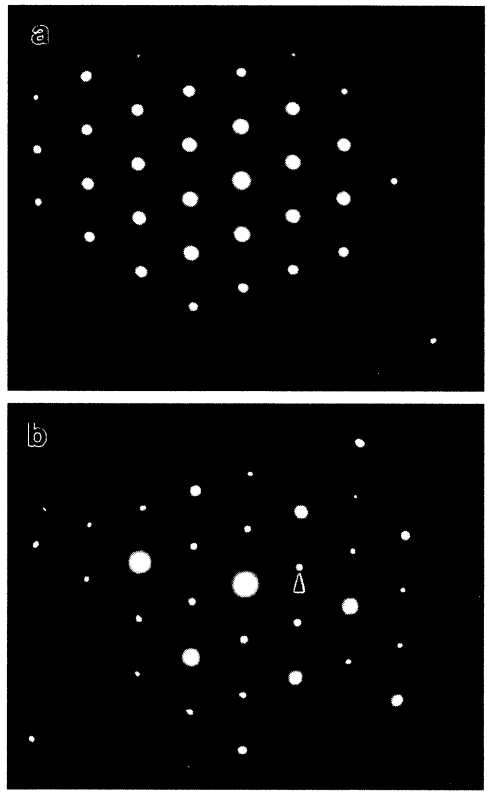

FIG. 5. SADPs taken along (a) [110] and (b) [114].

Figure 4(a) shows the plan view TEM bright field (BF) image. The NiMn grain size is around 3 μm and twins can be readily observed within the grains. The selected area diffraction pattern (SADP) in Fig. 4(b) reveals the twin plane to be fcc (111), which resulted in $(\bar{1}11)T$ and $(200)T$ twinned spots. These twins were formed to accommodate the lattice strain generated during the fcc$\rightarrow L1_0$ ordering reaction.[25,26]

In order to determine the crystal structure of NiMn, SADPs were taken along the [110] and [114] zone axes, wherein the degree of ordering can be determined by the presence of extra diffraction spots. In Fig. 5(a), the absence of (110) diffraction spot clearly shows the NiMn to be fcc. However, in the [114] pattern [Fig. 5(b)] ordering spots can be observed (arrow) which indicates that a certain amount of ordering is taking place.

(ii) *10 nm Mo/40 nm NiMn/30 nm NiFe/10 nm Ta/25 nm NiFeCr.* The exchange fields are listed in Table I. The presence of Ta is imperative to obtaining high exchange field as reflected by the low value in specimen D. On the other hand, the use of high substrate bias during Ta deposition appears to have an adverse effect on the strength of the exchange field in specimen C.

A (111) texture has developed in both the NiFe and NiMn films as shown in the x-ray diffraction spectra in Fig. 6. The intensity of the (111) NiMn peak is coupled to that of (111) NiFe, thus indicating an orientation relationship (OR) between them. Furthermore, the strength of the exchange field depends on the degree of the (111) texture. It is, however, infeasible to determine whether NiMn is ordered from the spectra because in both the fcc and $L1_0$ structures, there is only one (111) peak, i.e., the (111) peak does not split in tetragonal ordering.[20]

The cross-sectional TEM images of specimens A–D are shown in Figs. 7–10, respectively. The Ta layer is absent in D. In contrast, this layer is continuous in A–C. No granular nor diffraction contrast can be observed, which implies that the Ta film is amorphous. Strong columnar growth is also evident in both the NiMn and NiFe layers in these three specimens.

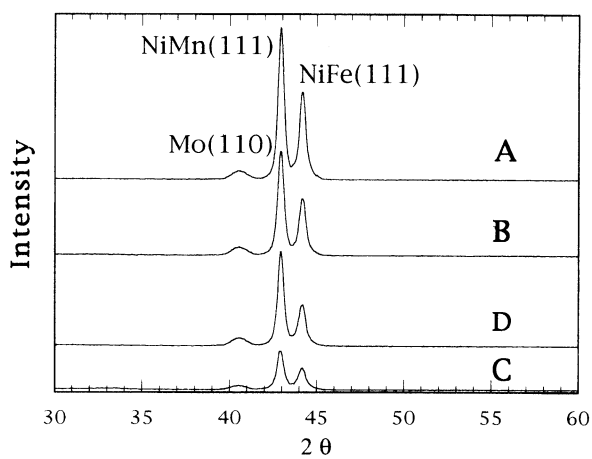

FIG. 6. X-ray diffraction spectra of A–D.

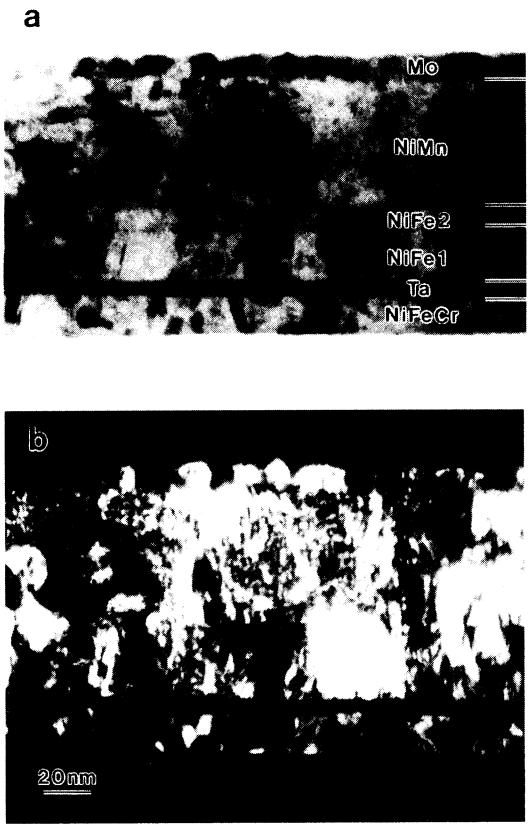

FIG. 7. (a) BF and (b) DF images of the cross section of specimen A.

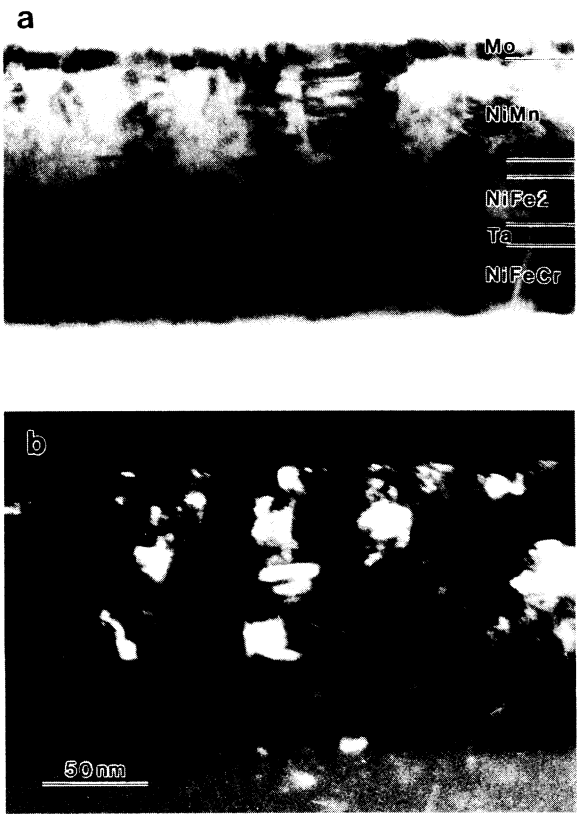

FIG. 9. (a) BF and (b) DF images of the cross section of specimen C.

The dark field (DF) image in Fig. 8(b) reveals a continuous columnar contrast through the NiFe and NiMn layers which supports the existence of an OR between them. Verification of this OR is provided by the SADP taken at the NiMn/NiFe interface of specimen C (Fig. 11), in which the NiFe (111) and the NiMn (111) diffraction spots line up (arrows). From the BF images, the NiFeCr film is polycrystalline and columnar growth is largely absent. Hence, the (111) texture is weak in this layer. In specimen D, NiFe grows directly on NiFeCr and it assumes the orientation of the NiFeCr grain as shown by the continuous diffraction contrast in the columns across the NiFe/NiFeCr interface [Fig. 10(b)]. This leads to weak columnar growth in the NiFe and NiMn layers and an underdeveloped (111) texture.

FIG. 8. BF images of the cross section of specimen B.

The interfaces between the various layers and the column boundaries in specimens A and D are sharp and flat, whereas they are almost indistinct in specimens B and C. This raises the possibility of chemical intermixing across the interfaces as a consequence of annealing.[27] A number of twins can be observed in the NiMn layer in the specimens. As stated earlier, they are generated during the ordering reaction. The highest density of twins can be found in specimens B and C, whereas the number declines in specimen A and they are largely absent in specimen D.

The cross-sectional atomic structures of specimen C are shown in Figs. 12 and 13. In Fig. 12(a), the NiFe (111) plane is parallel to the interface {NiFe $[1\bar{1}0]$ perpendicular to the plane of the paper}. Epitaxial growth is evident between the NiFe1 and NiFe2. The NiMn layer displays an atomic arrangement similar to that of NiFe and the lattice contrast is continuous across the NiMn/NiFe2 interface, revealing good epitaxial growth. A schematic of the atomic configuration is shown in Fig. 12(b) and the OR was determined to be

$$(111)_{\mathrm{NiFe}}//(111)_{\mathrm{NiMn}},\quad [1\bar{1}0]_{\mathrm{NiFe}},\quad [1\bar{1}0]_{\mathrm{NiMn}}.$$

The epitaxial growth between the two layers accounts for their correspondence in the x-ray spectra. By assuming a (111) NiFe interplanar spacing of 0.204 nm, the interplanar spacing of (111) NiMn planes was measured to be 0.2111 nm, which is larger than the equilibrium spacing for fct

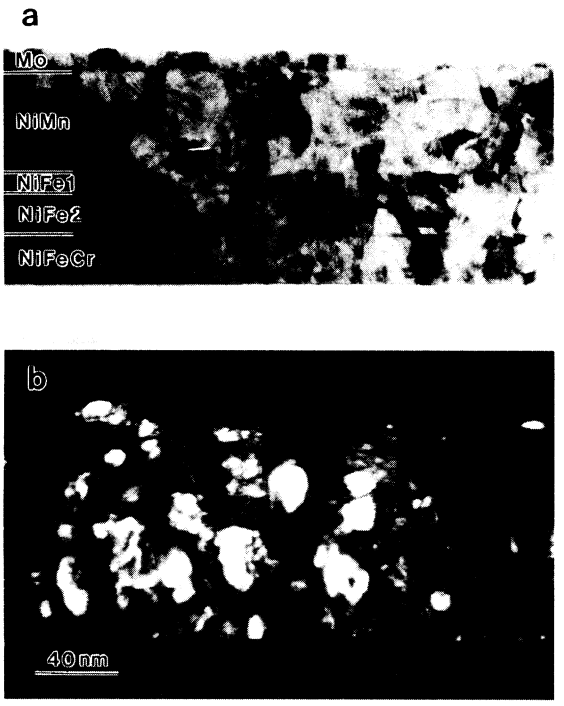

FIG. 10. (a) BF and (b) DF images of the cross section of specimen D.

NiMn. Misfit dislocations [arrows, Fig. 12(a)] comprising of NiFe $(11\bar{1})$ can be found at the interface resulting in a semicoherent interface. They were formed to accommodate the interfacial misfit due to the larger NiMn lattice.[28–30] The misfit dislocation spacing was measured to be 30 and 31 NiFe $(11\bar{1})$ planes, respectively. This can be compared to the calculated equilibrium misfit dislocation period

$$\mathbf{P}=\frac{\mathbf{d}_{\mathrm{NiMn}(111)}}{\mathbf{d}_{\mathrm{NiMn}(111)}-\mathbf{d}_{\mathrm{NiFe}(111)}},$$

which yields $\mathbf{P}=30$ ($\mathbf{d}_{\mathrm{NiMn}(111)}=0.211$ nm, $\mathbf{d}_{\mathrm{NiFe}(111)}=0.204$ nm. This indicates that the interface is in an equilibrium state. In addition, the NiMn (111) and $(11\bar{1})$ interplanar spacing are identical and their interplanar angle was measured to be 70.5°, the same as that for a fcc structure. This shows that the metastable fcc NiMn phase has been stabilized by fcc

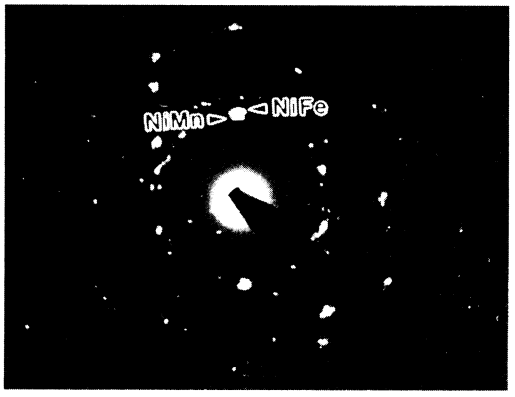

FIG. 11. SADP taken at the NiMn/NiFe interface of specimen A.

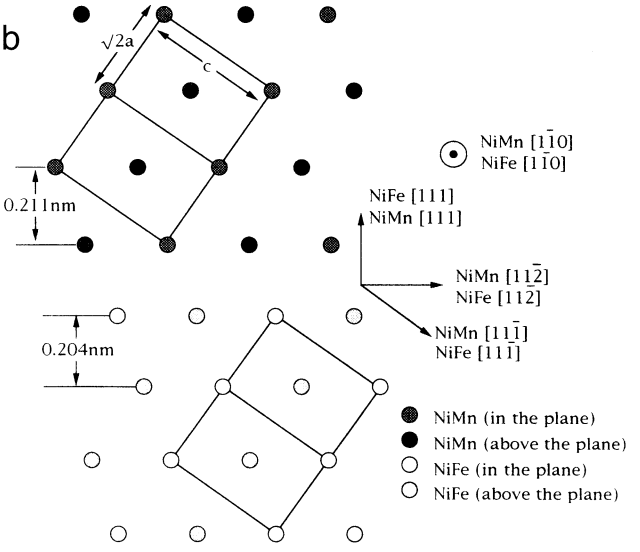

FIG. 12. (a) Atomic structure at the NiFe/NiMn interface in C. (b) A schematic of the atomic configuration across the interface.

NiFe at the interface and it has a lattice parameter of 0.365 nm. The (111) interplanar spacing for fcc and fct NiMn is 0.2111 and 0.2106 nm, respectively. Hence, it is difficult to differentiate the two structures by simply measuring the interplanar spacing. However, the {111} interplanar angle changes from 70.5° to 73.4° during the fcc→$L1_0$ transformation (Table II). Thus, it is possible to deduce the local crystal structure by measuring this interplanar angle. Furthermore, one can deduce the tetragonality of the crystal by measuring the **c/a** ratio from the atomic images [Fig. 12(b)].

Figure 13 shows the lattice image of the same NiMn column away from the interface. Twins can be observed which concurs with earlier observations. However, the {111}

TABLE II. Interplanar angle in fcc and fct NiMn.

Zone axis	hkl 1	hkl 2	Angle (fcc)	Angle (fct)
$[\bar{1}10]$	(111)	$(11\bar{1})$	70.52°	73.39°
$[10\bar{1}]$	(111)	$(1\bar{1}1)$	70.52°	69.98°
$[01\bar{1}]$	(111)	$(1\bar{1}\bar{1})$	109.48°	110.92°

interplanar angle was measured to be 72° instead of 70.5°. Thus, NiMn is no longer cubic away from the interface as local atomic ordering forces it to lose its cubic symmetry.

(iii) *10 nm Mo/40 nm NiMn/35 nm NiFe/10 nm Ta.* Figure 14 shows the x-ray diffraction spectra of specimens E and F, respectively. The increase in substrate bias during NiFe deposition helps to promote a strong NiFe (111) texture which leads to a similar enhancement in the NiMn (111) peak intensity for the aforementioned reasons. The NiFe (111) and NiMn (111) diffraction peak intensity in specimen E is nearly an order of magnitude higher than those in F.

The cross section and the corresponding SADP of specimen E are shown in Fig. 15. A strong columnar structure is once again evident in both NiFe and NiMn and a high density of NiMn (111) twins can be readily found (arrows). The numerous number of twins is also manifested in the SADP, which has a twinned [110] pattern similar to Fig. 4(b). Figure 16 shows similar images of F. Only a weak columnar structure is present in the NiFe layer and columns are virtually nonexistent in the NiMn layer. The Ta/Al_2O_3 interface is uneven and this roughness is replicated by NiFe and NiMn.

FIG. 13. Atomic structure in the NiMn layer away from the NiMn/NiFe interface in specimen C.

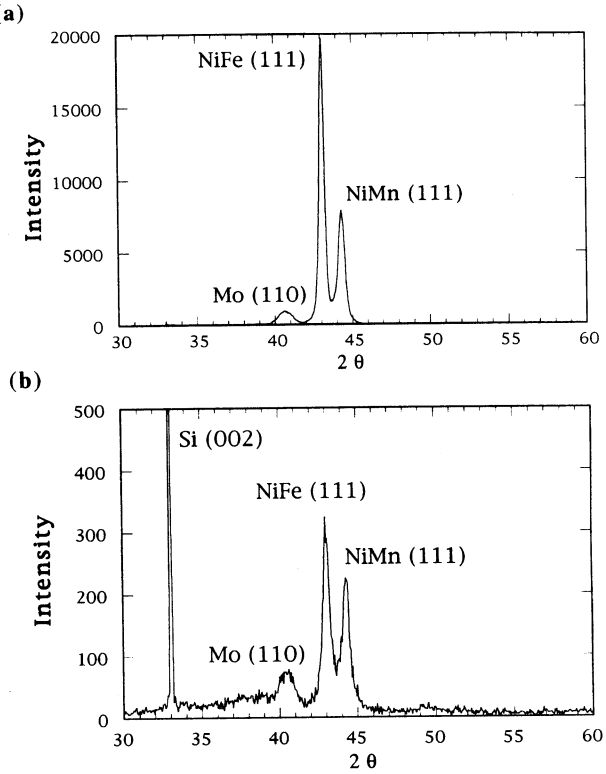

FIG. 14. X-ray diffraction spectra of (a) E and (b) F.

Due to the rough interface, columnar growth is discouraged and this absence of flat growing surface limits epitaxial growth between NiFe and NiMn. The absence of (111) texture is reflected in the SADP, in which no preferred alignment of lattice planes can be observed. Most importantly, this surface topography also precipitated the disappearance of NiMn twins in specimen F.

Figure 17 shows the atomic structure across a NiFe/Ta interface in specimen E. A strong NiFe (111) texture was clearly established at the interface leading to a columnar structure. The phenomenon can be related to the high substrate bias used during NiFe deposition and the good wetting behavior between NiFe and amorphous Ta.

The atomic structure of a NiMn grain column is shown in Fig. 18. A twin bisects the midsection of the grain and a heavily twinned region is present between areas B and C. Figure 19 shows the magnified images of the three areas denoted as A, B, and C. The angle {111} interplanar angles and the **c/a** ratios are listed in Table III. From the measurement results, the crystal is cubic in area C, whereas areas A and B have taken on tetragonality with the crystal having undergone twinning locally. Therefore, NiMn has become more tetragonal away from the interphase boundary, where the fcc stabilizing effect of fcc NiFe is less prominent. The lattice distortion from the ordering process is relieved by twinning of the crystal.

IV. DISCUSSION

A Ta underlayer is essential to attaining high exchange bias field as it provides an amorphous nucleation layer to help facilitate a NiFe (111) texture with strong columnar

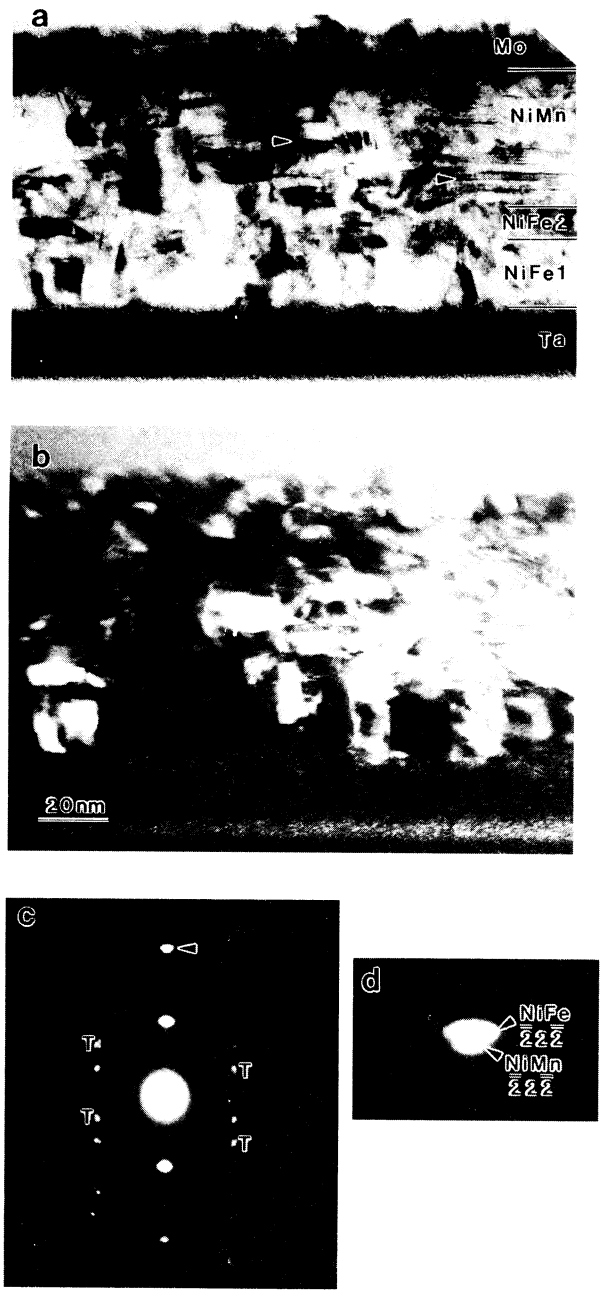

FIG. 15. (a) BF and (b) DF images of the cross section of specimen E. (c) and (d) SADP taken at the NiMn/NiFe interface of specimen E.

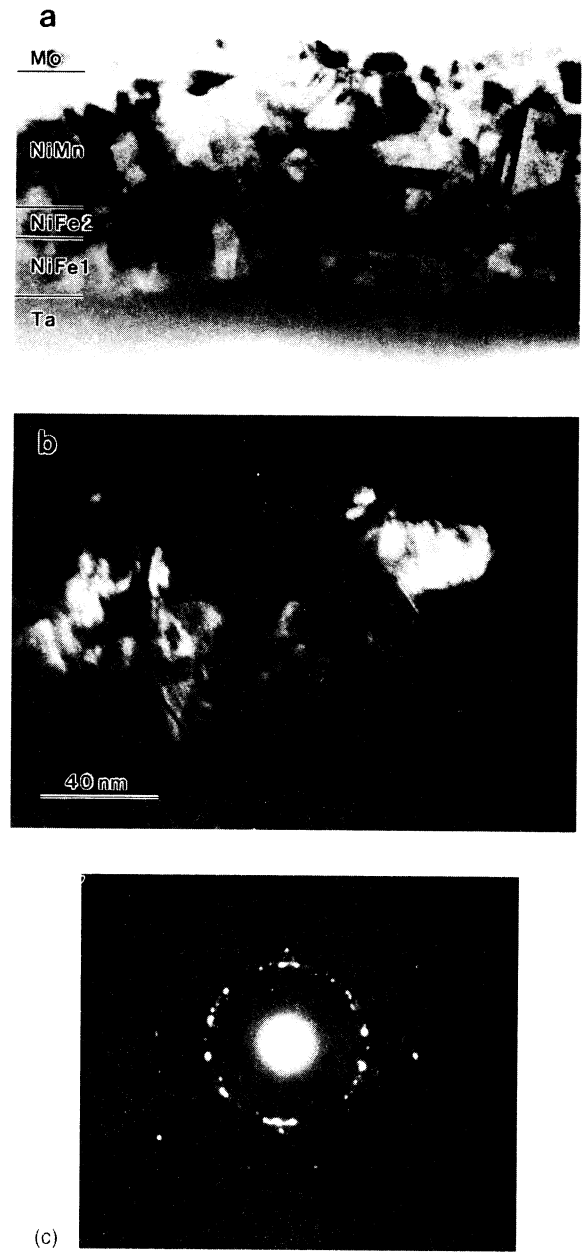

FIG. 16. (a) BF and (b) DF images of the cross-section of specimen F. (c) SADP taken at the NiMn/NiFe interface of specimen F.

growth. However, high substrate biasing during Ta deposition leads to a lower exchange field. It is well known that the use of substrate bias will reduce the density of crystalline defects in a growing film. An amorphous structure can be thought of as one with an infinite number of defects. Thus, the application of excessive substrate bias will lessen the degree of disorder in the Ta film, giving rise to a less amorphous nucleation layer for NiFe to grow on. This ultimately weakens the NiFe (111) texture.

The same analogy is applicable to explaining the effect of high substrate bias used during NiFe deposition on the strength of the exchange field. With the elevated substrate bias, the NiFe film has achieved better crystallinity, along with an enhancement in columnar growth and a smoother growing surface. All these factors helped promote the epitaxial growth of NiMn on NiFe. Furthermore, the high substrate bias also furnished a larger NiFe grain size which can play a role in raising the exchange field.

The epitaxial growth between NiFe and NiMn is indispensable in obtaining high exchange bias field. It has been observed from the microstructural investigation that the strength of the exchange field is closely related to the density of twins in the NiMn layer. This phenomenon can be understood by considering the effect of fcc NiFe on NiMn. At the interface, the epitaxial growth between NiMn and fcc NiFe helps to stabilize fcc NiMn during deposition. In the course of postdeposition annealing, local atomic ordering takes

FIG. 17. (a) and (b) Atomic structure NiFe/Ta interface in specimen E.

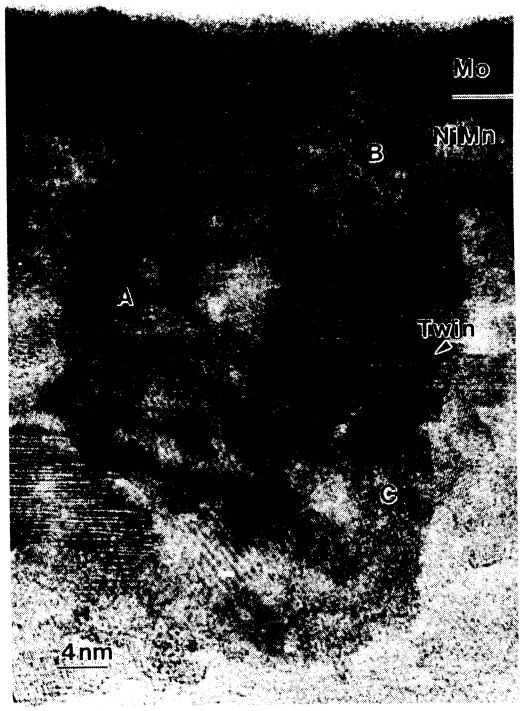

FIG. 18. HRTEM image of a NiMn column in E.

place within the NiMn film because the fcc phase is only a metastable structure. The result is the fcc→$L1_0$ transformation stated earlier. Associated with this ordering reaction is a modification in the NiMn lattice dimensions and this creates lattice strain, which in turn is relieved by twinning of the NiMn lattice. However, in the vicinity of the interface, fcc NiMn is stabilized by fcc NiFe. As a result, the ordering reaction is impeded locally as NiMn cannot be fully transformed into a $L1_0$ structure. Away from the interface, the stabilizing effect of NiFe is reduced and NiMn can undergo the transformation. Consequently, twins were generated and the lattice becomes more tetragonal. This accounts for the frequent observation of NiMn twins away from the NiMn/NiFe interface. In other words, the higher the twin density, the more ordered the NiMn film is. This also describes the reason for the low blocking temperature of 400 °C in the exchange biased film, compared to a Néel temperature of 800 °C in bulk, because full NiMn $L1_0$ ordering was not achieved at the interface. In addition, this may also explain the low exchange field in specimens with thin NiMn layers. In epitaxial growth, the metastable structure in the growing layer can be stabilized by the substrate/underlayer. In order to revert to its equilibrium structure, the growing film must reach a critical thickness in order to counterbalance this stabilizing influence.[28,29] Beyond this thickness, misfit dislocations are established to accommodate the lattice misfit, which came about as the top film progressively amasses a larger volume and creates a large strain state at the interface. In the present system, when the NiMn film is thin, the ordering reaction cannot proceed as fcc NiMn is stabilized by NiFe. Only when the NiMn film exceeds the critical thickness, then can it overcome the anchoring effect of NiFe and achieve partial ordering at the interface and attain the equilibrium $L1_0$ structure away from the interface.

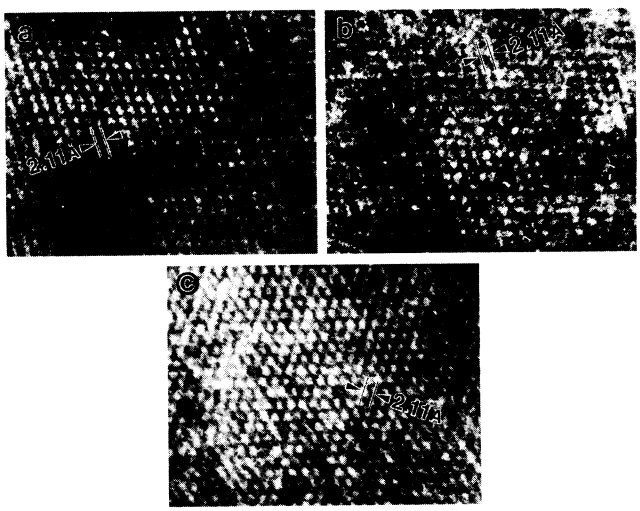

FIG. 19. (a)–(c) Magnified atomic structure of regions A, B, and C in Fig. 18.

TABLE III. The angle between (111) planes and the **c/a** ratio measured from areas A, B, and C in Fig. 19.

Area	{111}	c/a
A	74°	0.975
B	72°	0.95
C	71°	1.01

One solution to reduce the effect of fcc NiFe is to grow larger NiFe grains. Thus, the critical thickness can be achieved with a thinner NiMn film. This is in accord with the higher exchange fields possessed by the specimens with the NiFe films deposited with high substrate bias as they have a larger grain size. Furthermore, thinner NiMn is also advantageous because it reduces the shunt effect in spin valve.

V. CONCLUSIONS

The magnitude of the exchange bias field in the NiMn/NiFe system is closely associated with the strength of the (111) texture in the two layers. An amorphous Ta nucleation layer is necessary for the NiFe film to achieve a strong (111) texture and columnar growth. High substrate bias during NiFe deposition can also enhance this texture and improve surface smoothness. NiMn replicates the NiFe (111) texture through epitaxial growth and a cube on cube OR has been observed. At the interface, fcc NiMn is stabilized by the fcc NiFe layer which limits the ordering reaction. The degree of ordering at the interface affects both the strength of the exchange field and the blocking temperature. However, NiMn can undergo the fcc$\rightarrow L1_0$ transformation away from the interface as the effect of NiFe lessens. This resulted in (111) twins in the NiMn layer.

ACKNOWLEDGMENTS

The work was supported by a grant from Hitachi Metals Ltd. The authors would like to thank Dr. Simon Liao of AMC for his helpful discussions and Dr. Paul Frank of AMC for his assistance on this publication.

[1] C. Tsang, J. Appl. Phys. **55**, 2226 (1984).
[2] *Magnetic Recording Handbook*, edited by C. D. Mee and E. D. Daniels (McGraw-Hill, New York, 1990), p. 303.
[3] R. D. Hempstead, S. Krongelb, and D. A. Thompson, IEEE Trans. Magn. **MAG-14**, 521 (1978).
[4] C. Tsang and S. K. Decker, J. Appl. Phys. **52**, 2465 (1981).
[5] W. H. Meiklejohn and C. P. Bean, Phys. Rev. **102**, 1413 (1956).
[6] W. H. Meiklejohn and C. P. Bean, Phys. Rev. **105**, 904 (1957).
[7] J. S. Kouvel, C. D. Graham, Jr., and J. J. Becker, J. Appl. Phys. **29**, 518 (1958).
[8] D. Paccard, C. Schlenker, O. Massenet, R. Montmory, and A. Yelon, Phys. Status Solidi **16**, 301 (1966).
[9] B. Dieny, V. S. Speriosu, B. A. Gurney, S. S. P. Parkin, D. R. Wilhoit, K. P. Roche, S. Metin, D. T. Peterson, and S. Nadimi, J. Magn. Magn. Mater. **93**, 101 (1991).
[10] B. Dieny, V. S. Speriosu, S. Metin, S. S. P. Parkin, B. A. Gruney, P. Baumgaret, and D. R. Wilhoit, J. Appl. Phys. **69**, 4774 (1991).
[11] C. Hwang and T. A. Nguyen, Mater. Res. Soc. Symp. Proc. **232**, 211 (1991).
[12] C. Tsang, N. Heiman, and K. Lee, J. Appl. Phys. **52**, 2471 (1981).
[13] C. Tsang and K. Lee, J. Appl. Phys. **53**, 2605 (1982).
[14] C. Hwang, R. H. Geiss, and J. K. Howard, J. Appl. Phys. **64**, 6115 (1988).
[15] J. K. Howard and T. C. Huang, U.S. Patent No. 4 782 413.
[16] W. C. Cain, J. W. Lee, P. V. Koeppe, and M. H. Kryder, IEEE Trans. Magn. **MAG-24**, 2609 (1988).
[17] W. C. Cain and M. H. Kryder, IEEE Trans. Magn. **MAG-26**, 22 412 (1988).
[18] M. J. Carey and A. E. Berkowitz, Appl. Phys. Lett. **60**, 3060 (1992).
[19] M. J. Carey, A. E. Berkowitz, J. A. Borchers, and R. W. Erwin, Phys. Rev. B **47**, 9952 (1993).
[20] T. Lin, D. Mauri, N. Staud, C. Hwang, G. L. Gorman, and J. K. Howard, Appl. Phys. Lett. **65**, 1183 (1994).
[21] J. S. Kasper and J. S. Kouvel, J. Phys. Chem. Solids **11**, 231 (1959).
[22] L. Pai, E. Kren, G. Kadar, P. Szabo, and T. Tarnoczi, J. Appl. Phys. **39**, 538 (1968).
[23] E. Kern, E. Nagy, I. Nagy, L. Pal, and P. Szabo, J. Phys. Chem. Solids **29**, 101 (1968).
[24] V. E. Egorushkin, S. N. Kulkov, and S. E. Kulkov, Physica B **123**, 61 (1983).
[25] K. Adachi and C. W. Wayman, Metall. Trans. A **16**, 1567 (1985).
[26] K. Adachi and C. W. Wayman, Metall. Trans. A **16**, 1581 (1985).
[27] M. F. Toney, C. Tsang, and J. K. Howard, J. Appl. Phys. **70**, 6227 (1991).
[28] F. C. Frank and J. H. van der Merwe, Proc. R. Soc. London, Ser A **198**, 216 (1949).
[29] J. H. van der Merwe, J. Appl. Phys. **34**, 117 (1963).
[30] J. W. Matthews and A. E. Blakeslee, J. Cryst. Growth **27**, 118 (1974).